Gold–silica quantum rattles for multimodal imaging and therapy

Mathew Hembury[a,b,c], Ciro Chiappini[a,b,c], Sergio Bertazzo[a,b], Tammy L. Kalber[d], Glenna L. Drisko[e,f,g], Olumide Ogunlade[d,h], Simon Walker-Samuel[d], Katla Sai Krishna[i], Coline Jumeaux[a,b,c], Paul Beard[d,h], Challa S. S. R. Kumar[i], Alexandra E. Porter[a], Mark F. Lythgoe[d], Cédric Boissière[e,f,g], Clément Sanchez[e,f,g], and Molly M. Stevens[a,b,c,1]

[a]Department of Materials, [b]Institute of Biomedical Engineering, and [c]Department of Bioengineering, Imperial College London, London SW7 2AZ, United Kingdom; [d]Centre for Advanced Biomedical Imaging, Division of Medicine, University College London, London WC1E 6DD, United Kingdom; [e]Sorbonne Universités, Université Pierre et Marie Curie Paris 6, UMR 7574, Laboratoire de Chimie de la Matière Condensée de Paris, F-75005 Paris, France; [f]CNRS, UMR 7574, Laboratoire de Chimie de la Matière Condensée de Paris, F-75005 Paris, France; [g]Collège de France, UMR 7574, Laboratoire de Chimie de la Matière Condensée de Paris, F-75231 Paris, France; [h]Department of Medical Physics and Biomedical Engineering, University College London, London WC1E 6BT, United Kingdom; and [i]Center for Advanced Microstructures and Devices, Louisiana State University, Baton Rouge, LA 70806

Edited by Robert Langer, Massachusetts Institute of Technology, Cambridge, MA, and approved January 08, 2015 (received for review October 14, 2014)

Gold quantum dots exhibit distinctive optical and magnetic behaviors compared with larger gold nanoparticles. However, their unfavorable interaction with living systems and lack of stability in aqueous solvents has so far prevented their adoption in biology and medicine. Here, a simple synthetic pathway integrates gold quantum dots within a mesoporous silica shell, alongside larger gold nanoparticles within the shell's central cavity. This "quantum rattle" structure is stable in aqueous solutions, does not elicit cell toxicity, preserves the attractive near-infrared photonics and paramagnetism of gold quantum dots, and enhances the drug-carrier performance of the silica shell. In vivo, the quantum rattles reduced tumor burden in a single course of photothermal therapy while coupling three complementary imaging modalities: near-infrared fluorescence, photoacoustic, and magnetic resonance imaging. The incorporation of gold within the quantum rattles significantly enhanced the drug-carrier performance of the silica shell. This innovative material design based on the mutually beneficial interaction of gold and silica introduces the use of gold quantum dots for imaging and therapeutic applications.

nanomedicine | hybrid nanoparticle | cancer nanotechnology | gold quantum dots | mesoporous silica

Although gold's potential in nanotechnology has been recognized for many decades (1, 2), new insights into the unique properties of gold nanoparticles (NPs) of less than 2 nm have just recently started to emerge (3, 4). Such extremely small gold NPs could be transformative for a broad set of applications ranging from energy production and storage to catalysis and health care (3). As the size of gold NPs decreases below 2 nm, the quantization of their conduction band leads to molecule-like properties (3). These quantum-sized gold NPs (or gold quantum dots, AuQDs) absorb light in the near-infrared (NIR) biological window (650–900 nm) (2) and convert it into photons and heat (5). Furthermore, whereas bulk gold is diamagnetic, some AuQDs exhibit magnetic properties (4, 6). However, the clear therapeutic and imaging potential of AuQDs in vivo has been undermined by their unfavorable biointeractions and lack of stability in aqueous solvents (5, 7). In biological environments AuQDs tend to aggregate rapidly, reverting to larger gold nanoparticles (AuNPs) (8) and/or bind to protein, which negatively affects their cytotoxicity (7). To retain their advantages, AuQDs require a protective, stabilizing framework that allows proficient biological interactions.

Recently, new emphasis has been placed on hybrid NP systems, where multiple nanomaterials are assembled to create multimodal systems that exhibit the combined qualities of the component modules (9–11). These constructs promise to integrate various functionalities by incorporating different nanomaterials into a single, efficient, multimodal system (12, 13). However, these systems usually accumulate the specific functionalities of their component modules through multiple steps in their synthetic processes, thereby adding complexity at the expense of performance (11). Furthermore, certain functionalities are intrinsically difficult to combine, directing research efforts toward optimizing tradeoffs. Here, we propose taking a more holistic approach, whereby a simple, multifunctional design, centered on exploiting the advantages of AuQDs, induces a number of complementary emergent qualities for in vivo imaging and therapy.

We present a gold–silica rattle (quantum rattle, QR), consisting of a hollow mesoporous silica shell (HS) with two size domains of hydrophobic gold NPs: AuQDs (<2 nm) and larger AuNPs (>2 nm). The HS can host bioactive molecules and stabilizes the AuQDs, allowing them to retain their photonic and magnetic properties in aqueous media. The AuQDs are paramagnetic and absorb and emit light in the NIR biological window, enabling photothermal therapy (PTT) as well as multimodal live imaging (NIR fluorescence, magnetic, and photoacoustic imaging). The large hydrophobic gold surface area presented by the QRs seems to enhance the drug-carrying performance of the system by increasing the loading content and loading efficiency and prolonging the release of a drug payload. Here, we present direct evidence of the unique in vitro and in vivo therapeutic and imaging efficacy of this innovative hybrid system.

Significance

Therapeutic and diagnostic nanoparticles combine multiple functionalities to improve efficacy of treatment but often require assembling complex systems at the expense of overall performance. Here we present a simple strategy to synthesize a hybrid, rattle-like, gold–silica nanoparticle that very efficiently combines therapy and imaging in an animal model. The nanoparticle design is uniquely centered on enabling the use of gold quantum dots (<2 nm) in biological systems. The resulting nanoparticles are highly biocompatible and display emergent photonic and magnetic properties matching and in some instances outperforming state-of-the-art nanotechnology-based medical agents for each of the functionalities investigated, promising a tighter integration between imaging and therapy.

Author contributions: M.H., C.C., S.B., T.L.K., G.L.D., O.O., S.W.-S., K.S.K., P.B., C.S.S.R.K., A.E.P., M.F.L., C.B., C.S., and M.M.S. designed research; M.H., C.C., S.B., T.L.K., G.L.D., O.O., S.W.-S., K.S.K., and C.J. performed research; M.H., C.C., S.B., T.L.K., G.L.D., O.O., S.W.-S., K.S.K., C.J., P.B., C.S.S.R.K., A.E.P., M.F.L., C.B., C.S., and M.M.S. analyzed data; and M.H. and C.C. wrote the paper.

The authors declare no conflict of interest.

This article is a PNAS Direct Submission.

[1]To whom correspondence should be addressed. Email: m.stevens@imperial.ac.uk.

This article contains supporting information online at www.pnas.org/lookup/suppl/doi:10.1073/pnas.1419622112/-/DCSupplemental.

Downloaded at Palestinian Territory, occupied on December 4, 2021

www.manaraa.com

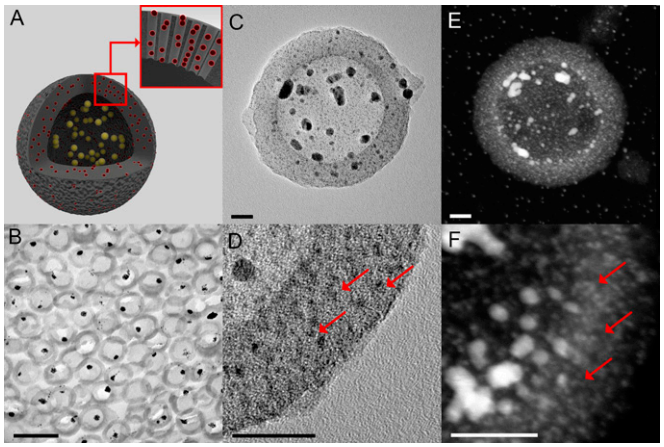

Fig. 1. The QR's morphology. (*A*) Schematic of a QR. QRs are composed of hollow mesoporous silica shells (HS, gray) hosting both AuQDs (red) inside their mesopores and gold nanoparticles AuNPs (yellow) inside their macrocavity. (*B*) Bright field TEM image of an ultrathin section of resin-embedded QRs, showing AuNPs within the mesoporous silica shells. (Scale bar, 0.2 μm.) (*C*) Bright field TEM image of a QR showing AuNPs within the cavity of the mesoporous silica shell. (Scale bar, 20 nm.) (*D*) Higher-magnification bright field TEM image of a QR silica shell showing the AuQDs (red arrows). (Scale bar, 20 nm.) (*E*) HAADF-STEM image of a QR highlighting the gold nanostructures within the particle. (Scale bar, 20 nm.) (*F*) Higher magnification HAADF-STEM image of a QR silica shell showing the AuQDs (red arrows). (Scale bar, 20 nm.)

Results and Discussion

We synthesized highly monodisperse Au@SiO_2 rattle-type particles (QRs) by nucleating gold within hollow mesoporous silica particles (14) (HS) in a one-step, one-phase synthesis (Fig. S1) (15). Chloro(triphenylphosphine) gold (I) was infused into the HS pores and macrocavity overnight. Subsequently, an alkanethiol ligand was added before initiating gold nucleation with an amine–borane complex as reducing agent. Instead of the more commonly used gold (III) salt, the QR synthesis used a gold (I) salt as a precursor. The nature of the gold salt was crucial to the QR synthesis because adaptations of methods using gold (III) chloride hydrate salt as metallic precursor invariably returned empty shells (Fig. S2). The amine–borane complex reducing agent preserved the integrity of the silica shell without showing signs of erosion or perforations following synthesis (Fig. S3).

The QRs were well-defined hollow spherical particles (~150 nm total diameter) with mesoporous silica shells (~25 nm thickness), hosting both AuQDs (<2 nm diameter) and AuNPs (average crystallite size 7.3 nm in diameter) as determined by transmission electron microscopy (TEM) and wide-angle X-ray scattering (WAXS) (Fig. 1 and Fig. S3). The presence of AuNPs in the macrocavity of the QRs was confirmed by imaging ultrathin sections of resin-embedded QRs (Fig. 1*B*). The AuQDs were confined within the mesopores of the silica shells (Fig. 1 *C* and *D*). High angle annular dark field scanning TEM (HAADF-STEM) was used to complement the bright field TEM study, highlighting all gold nanostructures present in the QRs (Fig. 1 *E* and *F*). The gold nanostructures within the QR accounted for 27% of its total weight (Fig. S4) and were equally distributed between AuNPs and AuQDs (13% and 14%, respectively), with an average of 16×10^3 AuQDs per QR (*Supporting Information*). The hydrophilic silica shell stabilized the otherwise water insoluble gold nanostructures, enabling the use of QRs in biological environments.

AuQDs Determine Photonic and Magnetic Properties of the QRs. The QRs displayed a distinct NIR extinction peak at 672 nm (Fig. 2*A*), as expected from the photonic properties of the AuQDs hosted within their mesopores (*Supporting Information*) (3, 16–18). This peak was absent from the HS or from the AuNPs synthesized using the same protocol in the absence of HS. Furthermore, the QRs' extinction peak at 672 nm excited a fluorescent emission mode at 827 nm (Fig. 2 *B* and *C*). To further confirm the photonic role of the AuQDs trapped within the mesopores, we synthesized mesoporous silica particles hosting only AuQDs (nonhollow QRs, NQRs). The NQRs presented the same extinction peak and fluorescent emission as the QRs in the NIR (Fig. S5) (3, 16–18). The QRs' quantum yield (2×10^{-4}) was comparable to the yields of other AuQDs reported in the literature (16). In addition to the high photostability granted by the AuQDs to the QRs (19), their large Stokes shift also provided a lower background signal and more flexible excitation options, which all contribute to improving the signal-to-noise ratio (20). Finally, the QRs' molar extinction coefficient at 672 nm (5.9×10^8 $M^{-1} \cdot cm^{-1}$, Fig. S6) was orders of magnitude higher than most organic dye or NP-based contrast agents and nearly matched that of gold nanorods (21).

The QRs exhibited a typical paramagnetic behavior with a magnetic moment at 2 K and 10,000 Oe equal to 0.009 μ_B per gold atom or 6554 μ_B per particle (as determined by superconductive quantum interference device (SQUID) measurements, Fig. 2*D*). Although many different and sometimes contradictory magnetic behaviors have been attributed to AuQDs (4), this result is consistent with our latest investigation of thiol-functionalized AuQDs of 25 atoms (6) and with density functional theory (DFT) calculations for AuQDs possessing a magnetic doublet with an odd number of electrons in the ground state (22). Assuming only the AuQDs exhibited a magnetic moment, the magnetism at 10,000 Oe per AuQD atom was equal to 0.017 μ_B. The magnetic moment per QR is relatively higher than those reported per AuNPs (Table S1) owing to the higher gold content in a single QR. The QRs exhibited

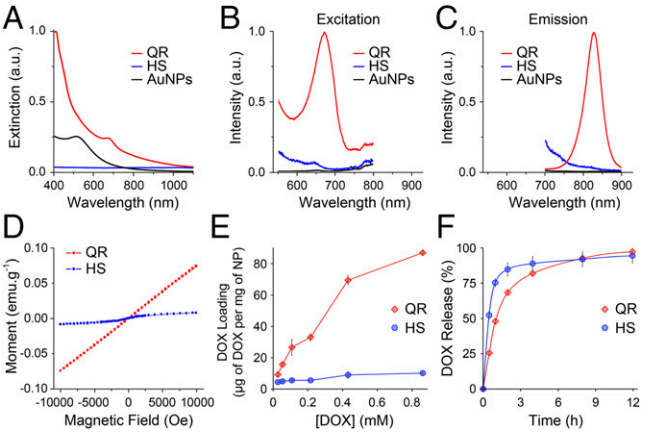

Fig. 2. QR properties: NIR optical, photoluminescent, magnetic properties, and drug-carrier performance. (*A*) Extinction spectrum of QRs (red) showing an extinction peak centered at 672 nm, which is absent for hollow mesoporous silica shells without gold (HS, blue) and spherical gold nanoparticles synthesized with the same method as the QRs but in the absence of hollow silica shells (AuNPs, black). (*B* and *C*) Photoluminescent excitation (*B*) and emission (*C*) spectra of QRs showing an excitation peak centered at 672 nm and an emission peak centered at 827 nm. Both excitation and emission peaks are absent from the HS (blue) and AuNPs (black) controls. Emission spectrum (λ_{ex} = 672 nm, red) and excitation spectrum (λ_{em} = 827 nm, gray). (*D*) The M vs. H magnetization curves of QRs (red) and HSs (blue) at 2 K showing that QRs exhibit paramagnetic behavior. (*E* and *F*) QR loading and release of DOX. (*E*) Plot of the DOX loading amount against DOX concentration of the loading solution showing up to ninefold increase in the amount of DOX loaded in the QRs (red) compared with the HSs (blue). (*F*) Drug release profile of QRs (red) compared with HSs (blue). The QRs seem to modulate the release kinetics, providing prolonged release compared with HSs. Error bars represent the SD of triplicate experiments.

Downloaded at Palestinian Territory, occupied on December 4, 2021
www.manaraa.com

paramagnetic behavior comparable to the commonly used multimodal magnetic resonance imaging MRI contrast agent, gadolinium oxide NPs, but lack their toxicity (23).

QRs Enhanced Drug-Carrier Performance. The QRs' potential as drug carriers was evaluated using the small-molecule drug doxorubicin (DOX). The saturation of DOX adsorption was evaluated for QRs, NQRs, and HSs in water using fluorescence spectroscopy. Whereas the NQR and HS controls both reached saturation when loaded with a 0.43 mM solution of DOX, the QRs had not reached maximum adsorption at the highest loading solution concentration investigated (0.86 mM) (Fig. 2*E* and Fig. S7*A*). Thermal gravimetric analysis (TGA) precisely quantified the DOX loading content, because fluorescence spectroscopy can underestimate DOX loading at high concentration owing to fluorescence quenching upon DOX stacking (24). The QRs exhibited enhanced drug loading (15.1% wt/wt) and loading efficiency (100%) compared with the mesoporous silica control (2.4% wt/wt loading content, 2.6% loading efficiency). By increasing the ratio of DOX to QRs to 1:1 (wt/wt), the QRs achieved a DOX loading content of 21.3% (wt/wt), albeit with a loading efficiency reduced to 40%. The high loading efficiency becomes particularly important when considering the cost effectiveness of treatment. At a nearly quantitative uptake of DOX from solution, the QRs' loading content was nearly twice that of optimized liposomal-DOX systems (7.8% wt/wt) as reported by one of the inventors of commercial Doxil/Caelyx (25). The HS mesoporous silica control displayed loading content at the low end of the large range of values reported in the literature (from 4% wt/wt to 122% wt/wt) (26, 27). This wide range of performance observed likely arises from differences in the silica surface chemistry, which determines the degree of interaction with the drug (28). The addition of hydrophobic gold nanostructures enhanced the adsorption of DOX, likely owing to chemical modifications induced to the silica surface alongside specific adsorption onto the large available gold surface (AuNPs and AuQDs).

The DOX-loaded QRs and NQRs prolonged the release of the drug payload when compared with the DOX-loaded HSs (Fig. 2*F* and Fig. S7*B*). By hosting AuQDs, QRs and NQRs presented a more tortuous pore structure than HSs as well as an enhanced affinity for DOX. Consequently, the QRs extended the release of DOX to 12 h from 4 h observed for HS. However, the similar release profiles for the QRs and NQRs indicate that the macrocavity did not affect the release kinetics (Fig. S7*B*). Diffusion-based models provided a poor fit to the drug release profiles of all drug-loaded particles. However, the pseudo-second-order sorption model (29) fitted the nonlinear data with R^2 values of 0.99 (Fig. S7*B*). The rate-limiting step in this pseudo-second-order model is from chemical desorption, indicating a relatively strong attraction between the substrates and DOX.

The cellular uptake and the cytotoxicity of DOX-loaded QRs were investigated to establish the drug delivery performance of the QRs in vitro over the concentration range of 0.57 nM to 57 μM (Fig. S8). Cells internalized DOX-loaded QRs with the same efficiency as free DOX, resulting in a similar cytotoxicity profile, with an IC_{50} of 1,468 nM and 1,229 nM for DOX and DOX-loaded QRs, respectively. The drug-loading performance of the QRs coupled to their targeting potential and the biodegradability of the silica shells (30) make the QRs attractive candidates for drug delivery applications.

QRs Enable Multimodal Imaging. As a first step toward assessing the QRs' potential in health care, in vitro testing demonstrated that the QRs were internalized as a single agent by cells and did not exhibit cytotoxicity over several days (Fig. 3 and Fig. S9). The fluorescent images and reconstructed 3D movie showed QRs localized within vesicular structures inside the cells' cytoplasm and accumulating in the perinuclear region (Fig. 3 *A* and *B* and Movie S1). This is compatible with endocytotic processes that internalize particles and traffic them through the endolysosomal system to finally accumulate in the perinuclear area (31). Additionally, TEM of ultrathin sections showed that the QRs were localized in large clusters within vesicles inside the cytoplasm (Fig. 3 *C* and *D*). The AuNPs were clearly surrounded by a silica shell, which seemed to include small, darker spots, which could represent the AuQDs. Finally, energy-dispersive X-ray spectroscopy (EDS) (Fig. S10) confirmed the presence of gold and silicon, providing further indication toward the QRs' internalization as a single agent.

To evaluate their performance as combined agents for multimodal imaging and therapy, the QRs were tested in a murine colorectal carcinoma tumor model (LS174T, Fig. 4). Multimodal imaging exploits the advantages of complementary imaging techniques while compensating each other's limitations. By combining optical, magnetic, and photoacoustic imaging (PAI), the QRs can offer high spatial resolution in three dimensions (MRI and PAI), excellent contrast between soft tissues (MRI), high sensitivity (fluorescent imaging, FLI), and high temporal resolution (within seconds) at low cost (FLI), as well as the ability to image across a range of scales (millimeter to hundreds of microns for MRI and PAI respectively) (13, 32, 33).

When imaged by FLI, QR-treated tumors showed focal points of NIR fluorescence colocalized with the QRs (Fig. 4*A*). In contrast to the QR-treated tumors, the HS-treated control tumors did not fluoresce. The paramagnetism of the QRs enabled their use in vivo as a contrast agent for MRI. The QRs provided a clear

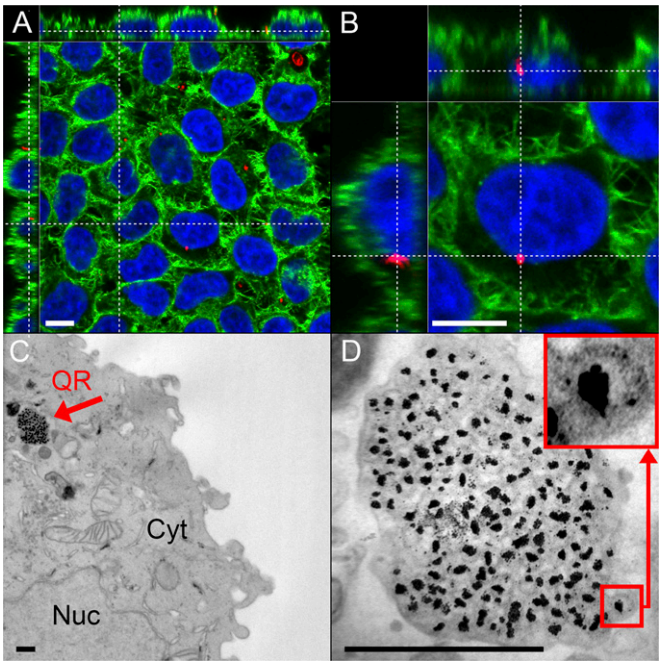

Fig. 3. QR interaction with cells: internalization and NIR fluorescence in vitro. (*A* and *B*) Laser confocal scanning microscopy images of HeLa cells incubated for 1 d with QRs, which are imaged through their native fluorescence (red). Cells are stained for F-actin (AF488 phalloidin, green) and nucleus (DAPI, blue). QRs are localized by their native fluorescence within the cells and are found to accumulate in the cytoplasm and perinuclear region. (Scale bars, 10 μm.) Cell overview (*A*) and close-up of one HeLa cell (*B*), showing accumulation of QRs in the perinuclear region. An animated 3D reconstruction of the data set visualized in *A* and *B* is available as Movie S1. (*C* and *D*) Bright field TEMs of ultrathin sections of HeLa cells incubated with QRs for 1 d showing the internalization of the entire QR structure. (Scale bars, 500 nm.) (*C*) Cell overview (Cyt, cytoplasm; Nuc, nucleus). The red arrow points to the internalized QRs being trafficked within a vesicle. (*D*) Higher-magnification bright field TEM image of the QR agglomerate inside a vesicle. (*Inset*) An individual QR.

Downloaded at Palestinian Territory, occupied on December 4, 2021

www.manaraa.com

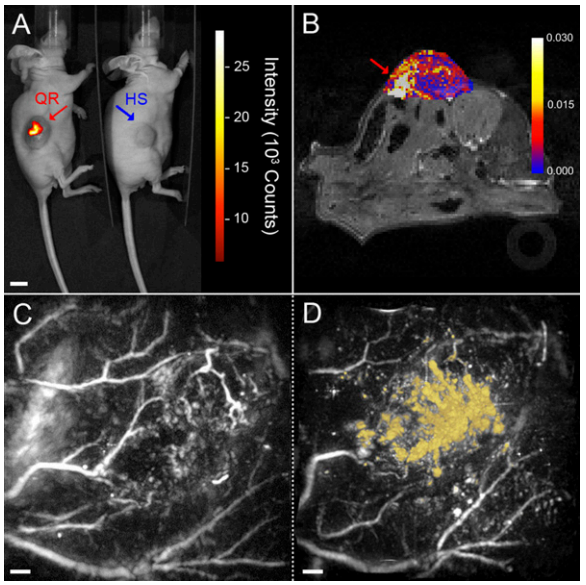

Fig. 4. Multimodal in vivo imaging of QRs in a LS174T-luc tumor model in CD1 nu/nu mice. (*A*) NIR fluorescence image showing focal points of fluorescent intensity where QRs (red) were injected in the tumor compared with nonfluorescent hollow mesoporous silica shells control (HS, blue). (Scale bar, 10 mm.) (*B*) Image showing the change in longitudinal relaxation rate (R_1) from baseline following injection of QRs. A focal point of increased R_1 is visible inside the tumor (red arrow), coinciding with the point of injection. (*C* and *D*) Horizontal maximum intensity projections (*x*–*y*) of 3D photoacoustic images ($14 \times 14 \times 6$ mm^3) of a tumor acquired at 670 nm before (*C*) and after (*D*) injection of QRs. The contrast provided by the QRs in the postinjection image is false-colored yellow. An animated volume-rendered image of the data set visualized in *D* is also available as Movie S2. (Scale bars, 1 mm.)

contrast within the tumor mass with a focal point of increase in longitudinal relaxation rate (R_1) compared with the baseline, colocalized with the QRs (Fig. 4*B*). The high spatial resolution offered by MRI complements the high sensitivity of fluorescent imaging to provide a more complete picture of the agent's distribution in the tumor (34). The NIR optical absorption of the QRs enabled PAI (35). Posttreatment photoacoustic images acquired at 670 nm showed a distinct QR signal within the tumor mass owing to the differential absorption contrast existing between QRs and hemoglobin at this wavelength (Fig. 4 *C* and *D* and Movie S2). The strong PAI contrast exhibited by hemoglobin means that PAI can also precisely image the vasculature (36) allowing the localization of the QRs relative to the tumor vascular network.

QRs Mediate Photothermal Therapy. The QRs induced cell killing in vitro, which suggested a potential for efficient and accurate QR-mediated PTT (Fig. 5). Indeed, QR treatment on HeLa cells displayed dose-dependent cell death upon NIR light irradiation (671 nm, 38 W·cm^{-2}) that saturated after 10 min. Cell death was almost entirely localized within the laser spot and reached 97% of the cell population. Appropriate controls demonstrated the need for both QRs and NIR light to induce cell death.

In vivo QR-mediated treatment was examined using luciferase-positive colorectal carcinoma cells (LS174T-luc) grown as an s.c. tumor model in mice (Fig. 6). LS174T cells were transfected for stable expression of luciferase, allowing luciferin-based, live bioluminescence imaging of tumor growth. Following the direct injection of either QRs or HSs (100 μL, 5.7×10^{12} particle·mL^{-1}), a thermal camera monitored the tumor temperature to reveal that upon irradiation with NIR light (671 nm, 0.9 W·cm^{-2}) QR-treated tumors reached a maximum average temperature of 51.6 ± 0.7 °C, which was a 15.1 ± 0.8 °C increase above the core body temperature. In contrast, with the HS-treated controls the maximum temperature was 39.7 ± 0.8 °C, which was a 3.2 ± 1.0 °C increase over the core body temperature (Fig. 6 *A* and *B*). This slight warming effect was due to the laser and was in good agreement with previous findings on the interaction of light with tissue (37). QR-mediated treatment raised temperatures well above the damage threshold needed to induce irreversible tissue damage (38) with laser dosages fivefold less than those reported in earlier studies for other PTT agents (32, 39). The tissue heating levels observed in the HS controls, however, were insufficient to induce damage (38). The interstitial accumulation within the tumor at the high levels used in this study is safely attainable by i.v. injections and passive targeting. Assuming a passive accumulation rate of ~5% (40), the i.v. 333 mg·kg^{-1} dose (equivalent to 243 mg·kg^{-1} and 90 mg·kg^{-1} of silica and gold, respectively) required to achieve the same amount of particles injected directly in the tumor lies below the established 500 mg·kg^{-1} toxic dose for a single injection of mesoporous hollow silica particles (41) or 1,000 mg·kg^{-1} for gold nanoparticles (42, 43).

The damage induced by the QR treatment was quantified through the bioluminescent intensity of the luciferase-transduced tumor cells immediately before and 24 h after treatment (Fig. 6*C*). One day following treatment, the luciferin signal intensity significantly decreased by −55% ($P < 0.05$) within the laser-irradiated area of QR-treated tumors. Instead, the same laser-irradiated area within the HS-treated tumors showed a bioluminescence signal increase of +3%. These findings correlated well with gross pathology at day one, in which characteristic zones of ulceration were visible in QR-treated tumors but not in HS-treated controls (Fig. 6*D*). Underlying necrosis was present in all tumors owing to tumor growth and the injection route of the particles. However, well-defined cone shapes of tissue necrosis directly under the NIR laser beam were seen in all QR-treated tumors and absent in the HS-treated controls. The average cone base diameter was approximately equal to the laser spot size (5 mm) and ~3 mm deep. Finally, whereas the immediate tumor periphery was ablated in the QR-treated tumors it remained continuous and intact in the HS-treated controls.

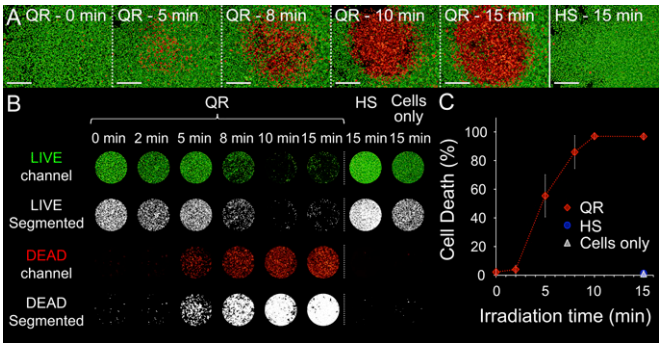

Fig. 5. QRs mediate localized hyperthermia in vitro. LIVE/DEAD assays on HeLa cells (live cells in green, dead cells in red) treated with NIR laser light (671 nm, 38 W·cm^{-2}, spot size ~1 mm). (*A*) Representative LIVE/DEAD microscopy images of cells treated for 1 d with either QRs and irradiated for 0, 5, 8, 10, and 15 min or hollow mesoporous silica shells (HS) and irradiated for 15 min as negative control. (Scale bars, 500 μm.) (*B*) Segmentation and quantification of the LIVE/DEAD assays. Image series showing the area under the laser spot (~1 mm) for cells treated with QRs or HSs and cell media only (i.e., no particle) for different irradiation times. The binary image series obtained from segmentation were used to quantify the LIVE/DEAD assays. The percentage of cell death was calculated as the sum of the DEAD binary image matrix and normalized to the sum of LIVE and DEAD binary matrices. (*C*) Plot of cell death vs. irradiation time. Cell death under the laser spot is proportional to the dose between 2 and 10 min, reaching 97% cell death after 10 min. Error bars represent the SDs of quadruplicate experiments.

Downloaded at Palestinian Territory, occupied on December 4, 2021
www.manaraa.com

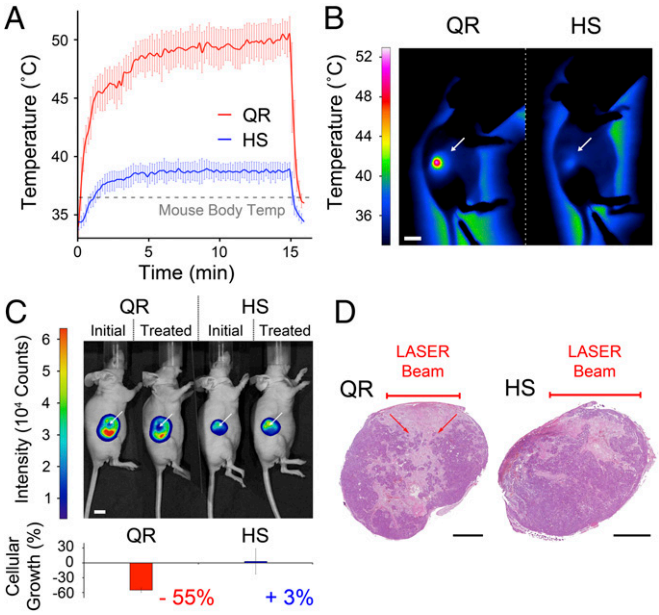

Fig. 6. QR-mediated therapy performance in a LS174T-luc s.c. tumor model in CD1 nu/nu mice. (*A*) Temperature profiles of tumors treated with either QRs (red) or hollow mesoporous silica shells (HS, blue) (100 μL, 5.7×10^{12} particle·mL^{-1}), monitored with a thermal camera, showing a 15.1 °C temperature increase from the mouse body temperature in the QR-treated samples upon irradiation with a 671-nm laser (0.9 W·cm^{-2}, 5-mm spot) compared with 3.2 °C for the HS-treated controls. The QR-treated areas reached temperatures above 51 °C after less than 1 min irradiation, whereas HS-treated control areas plateau at 39 °C after ∼5 min. (*B*) Thermal images obtained at 15 min of NIR light treatment of flank tumors (white arrows) treated with either QRs or HSs showing temperatures above 50 °C for QR-treated areas compared with temperatures below 40 °C for HS controls. (Scale bar, 10 mm.) (*C*) Representative bioluminescence images and quantification of the luciferin signal intensity of tumors treated with either QRs or HSs, before and after NIR light irradiation. The QR-treated tumors show a −55% decrease in luciferin activity compared with HS controls within the NIR light-exposed area of the tumor (white arrows) ($P < 0.05$). (Scale bar, 10 mm.) (*D*) Representative hematoxylin/eosin staining of sections of QR- or HS-treated tumors irradiated for 15 min with NIR light (671 nm, 0.9 W·cm^{-2}, spot size ∼5 mm) showing a characteristic cone-shaped zone of necrosis directly under the laser beam for the QR-treated tumor (red arrows), which is absent in the HS-treated control. Error bars in all charts represent the SDs of triplicate experiments. (Scale bars, 2 mm.)

The QRs display potential for cancer imaging and treatment. Additional investigations of the QRs' biodistribution, safety, and administration strategies in a preclinical setting will be necessary to assess QRs' performance as an anticancer agent in the clinic. Notwithstanding, the QRs are expected to perform in line with bare silica NP-based therapeutic/diagnostic systems both in terms of biodistribution and therapeutic effect (41). As silica particles, the QRs are easily amenable to biofunctionalization that can improve both their biodistribution and their therapeutic efficacy to clinically relevant degrees (44).

Conclusion

Optimizing hybrid multifunctional nanomaterials is a nontrivial undertaking, subject to many and varied considerations, which often requires adoption of design compromises (11). In contrast, we propose a multifunctional agent with emergent properties arising from a simple synergistic design, which enhanced the performance of its constituent components. The QRs' design stabilized AuQDs in the biological environment, allowing them to retain their photonic activity and paramagnetism, thereby enabling their use for multimodal imaging and therapy. Many hybrid NP systems are attempting to achieve mutually beneficial effects; however, complex constraints inherent within their design have limited their performance (32, 39). Here, all of the components of the QRs act in concert to optimize the multiple tasks at hand: tumor burden reduction, increasing the retention time of a drug payload, and enabling efficient multimodal imaging in vivo. In a broader context, the QRs' ability to stabilize a large number of AuQDs that are photonically and magnetically active could carry transformative potential for catalysis as well as label-free chemical and biochemical detection.

Materials and Methods

Synthesis of QRs. Detailed information regarding synthesis of the hollow mesoporous silica shells (HSs) can be found in *Supporting Information*. The QRs were obtained by infusing the HSs with gold precursors using a one-step, one-phase method (Fig. S1) (15). Chloro(triphenylphosphine) gold (I) salt (0.45 mmol) and HSs (100 mg) were suspended in chloroform (25 mL) and left to mix overnight at room temperature. The next day, 1-octanethiol (0.9 mmol) was added to the gold–silica suspension and left to mix for 20 min. A solution of borane *tert*-butylamine complex (4.5 mmol) was then prepared in chloroform (15 mL) and added to the gold–silica–thiol solution while mixing in a round-bottom flask. The reaction vessel was then equipped with a condensation column and transferred to a preheated 55 °C oil bath. The solution was left to react for 1 h. After cooling the solution to room temperature, diethyl ether (250 mL) was added and the particles were left to settle overnight at 4 °C. The supernatant was removed and the particles were washed and centrifuged three times at 236 × *g* for 8 min in diethyl ether and twice at 4,440 × *g* for 20 min in ethanol/chloroform (1:20) before leaving to dry at room temperature.

Particle Morphology and Composition. TEM images of the particles were acquired using a JEOL 2010 TEM equipped with a Gatan camera and an energy-dispersive X-ray spectroscopy detector (Oxford Instrument) operated at an accelerating voltage of 200 kV. High-magnification TEM images and HAADF-STEM images of the particles were acquired on a Gatan camera using a FEI TITAN 80/300 STEM/TEM operated at an accelerating voltage of 200 kV. TEM images of ultrathin sections of resin-embedded QRs (*Supporting Information*) were acquired using a JEOL 2000 TEM operated at 120 kV.

Photonic and Magnetic Characterization. UV-visible measurements were collected using a PerkinElmer Lambda 25 UV-visible spectrophotometer while steady-state photoluminescence measurements were collected using a Horiba Scientific Fluorolog-3 (FL3-21) spectrophotometer. Magnetic measurements were carried out using a Quantum Design MPMS-5S SQUID magnetometer. The field dependence of the magnetization (M vs. H) was measured for both QRs and HSs samples at 2 K.

Drug Loading and Release Studies. Detailed information regarding the DOX loading and release studies can be found in *Supporting Information*. Briefly, after loading the DOX into the particles overnight, the fluorescence emission of the loaded particles was monitored at 590 nm with an excitation wavelength set at 470 nm using a microplate reader (SpectraMax M5) and quantified against a standard curve. For the release studies, after washing and resuspending the DOX-loaded particles in PBS (pH 7.4), the supernatant of the samples were collected at different time points and their fluorescence was measured as described above. Both experiments were run in triplicate and the results are presented as averages ± SD.

QR Internalization Studies. Detailed information regarding the culture of the human cervical cancer HeLa cells as well as the laser confocal scanning microscopy and electron microscopy internalization studies can be found in *Supporting Information*.

Assessment of the QR's Photothermal Performance in Vitro. Detailed information regarding the LIVE/DEAD assay can be found in *Supporting Information*. After obtaining the LIVE/DEAD images, they were segmented to quantify the QR-mediated cell death. The irradiated cell population was confined to a 1-mm disk centered on the laser spot by masking. Both LIVE and DEAD channels were then segmented using MATLAB R2012a (MathWorks) into binary images. The percentage cell death was obtained by calculating the sum of the binary image matrices and normalizing the DEAD channel value over the total of LIVE plus DEAD channels. The experiment was run in quadruplicate and the results are presented as averages ± SD.

Downloaded at Palestinian Territory, occupied on December 4, 2021

www.manaraa.com

Animal Model and Tumor Inoculation. LS174T human colorectal carcinoma cells were stably transduced to express firefly luciferase coexpressing truncated CD34 (45) (LS174T-luc) in Martin Pule's laboratory. All animal studies were approved by the University College London Biological Services Ethical Review Committee and licensed under the U.K. Home Office regulations and the Guidance for the Operation of Animals (Scientific Procedures) Act 1986 (Home Office, London, United Kingdom). Seven female adult (6–8 wk) CD1 nu/nu mice (Charles Rivers) were anesthetized using 2% (vol/vol) isoflurane in O_2 and received s.c. injections of 5×10^6 LS174T-luc cells in 100 μL serum-free DMEM into the right flank. Animal weights and tumor volumes were recorded every 2 d using calipers until they reached 500 mm^3.

QR As Imaging Agent in Vivo. Detailed information regarding the FLI, MRI, and PAI, including sample preparation and acquisition parameters, can be found in *Supporting Information*. Briefly, mice injected with QRs or HSs were imaged with an IVIS Lumina II Bioluminescent scanner (Caliper Life Sciences) set to fluorescence mode for FLI; a 9.4T Agilent VNMRS scanner with a 39 mm radiofrequency coil (Rapid Biomedical) for MRI; and an all-optical, backward mode, planar photoacoustic scanner based upon a Fabry–Perot (FP) polymer film ultrasound sensor for PAI (36).

QR's Performance As Therapy Agent in Vivo. Detailed information regarding the QR-mediated therapy performance in a LS174T-luc s.c. tumor model in CD1 nu/nu mice can be found in *Supporting Information*. Briefly, mice injected with QRs or HSs (100 μL, 5.7×10^{12} particle·mL^{-1}, QR $n = 3$, HS $n = 3$) were imaged for bioluminescence expression with an IVIS Lumina II Bioluminescent scanner before and 24 h after exposure to NIR light (671 nm, 0.9 W·cm^{-2}, 5-mm spot diameter, 15 min). During the NIR light exposure the temperature profiles were monitored by using an Infratec VarioCAM hr 780 IR thermal camera. The mice were then killed by schedule 1 method and the tumors were removed for histology. Tumors were fixed in 4% (vol/vol) formalin for 4 h at 4 °C and then incubated overnight in 15% (wt/vol) sucrose in PBS at 4 °C. Tissue was dehydrated in 70% (vol/vol) ethanol and embedded in paraffin. Sections were cut at 5 μm and then stained with hematoxylin for 1 min and eosin for 30 s and images were obtained using a Hamamatsu NanoZoomer 2.0-HT Slide Scanner (Hamamatsu Japan) with NanoZoomer Digital Pathology NDP. view software (Hamamatsu Japan).

ACKNOWLEDGMENTS. The authors thank M. Selmane for his help in small- and wide-angle X-ray scattering characterization, R. Ghatrora and A. Jathoul for helping with the fluorescence live imaging experiment, P. Southern for lending the thermal camera, and M. Pule for providing the transduced human colorectal cell line LS174T-luc. M.H. was supported by a studentship from the Engineering and Physical Sciences Research Council (EPSRC) and a fellowship from the Rosetrees Trust. C.J. was supported by a studentship from the Rosetrees Trust. M.M.S. acknowledges financial support from the Rosetrees Trust and EPSRC Grant EP/K020641/1. A.E.P. acknowledges support from a European Research Council starting grant, (project number 257182). K.S.K. and C.S.S.R.K. thank the US Department of Energy (Award DE-SC0001058) for partial funding and Louisiana Board of Regents for an equipment grant [LEQSF (2008-10)-ENH-TR-07]. T.L.K. was supported by an EPSRC Early Career fellowship (EP/L006472/1), and S.W.-S. was supported by a Wellcome Trust Senior Research fellowship (WT100247MA). O.O., P.B., and M.F.L. acknowledge support from the King's College London and University College London (UCL) Comprehensive Cancer Imaging Centre Cancer Research UK (CR-UK) and the EPSRC, in association with the Medical Research Council (MRC) and Department of Health (DoH) (United Kingdom). M.F.L. also received funding from the UK Regenerative Medicine Platform Safety Hub (MRC: MR/K026739/1). O.O. and P.B. further acknowledge support from European Union Project Functional Anatomical Molecular Optical Screening (FAMOS) (FP7 ICT, Contract 317744). G.L.D., C.B., and C.S. acknowledge financial support from Collège de France and CNRS.

1. Boisselier E, Astruc D (2009) Gold nanoparticles in nanomedicine: Preparations, imaging, diagnostics, therapies and toxicity. *Chem Soc Rev* 38(6):1759–1782.
2. Jain PK, Huang X, El-Sayed IH, El-Sayed MA (2008) Noble metals on the nanoscale: Optical and photothermal properties and some applications in imaging, sensing, biology, and medicine. *Acc Chem Res* 41(12):1578–1586.
3. Qian H, Zhu M, Wu Z, Jin R (2012) Quantum sized gold nanoclusters with atomic precision. *Acc Chem Res* 45(9):1470–1479.
4. Nealon GL, et al. (2012) Magnetism in gold nanoparticles. *Nanoscale* 4(17):5244–5258.
5. Shang L, Dong S, Nienhaus GU (2011) Ultra-small fluorescent metal nanoclusters: Synthesis and biological applications. *Nano Today* 6(4):401–418.
6. Krishna KS, Tarakeshwar P, Mujica V, Kumar CSSR (2014) Chemically induced magnetism in atomically precise gold clusters. *Small* 10(5):907–911.
7. Shang L, et al. (2012) Effect of protein adsorption on the fluorescence of ultrasmall gold nanoclusters. *Small* 8(5):661–665.
8. Samanta A, Dhar BB, Devi RN (2012) Ultrasmall gold cluster arrays encapsulated in silica nanospheres: Applications in fluorescence imaging and catalysis. *J Phys Chem C* 116(2):1748–1754.
9. Drisko GL, Sanchez C (2012) Hybridization in materials science - Evolution, current state, and future aspirations. *Eur J Inorg Chem* 2012(32):5097–5105.
10. Sanchez C, Belleville P, Popall M, Nicole L (2011) Applications of advanced hybrid organic-inorganic nanomaterials: from laboratory to market. *Chem Soc Rev* 40(2):696–753.
11. Sailor MJ, Park J-H (2012) Hybrid nanoparticles for detection and treatment of cancer. *Adv Mater* 24(28):3779–3802.
12. Melancon MP, Zhou M, Li C (2011) Cancer theranostics with near-infrared light-activatable multimodal nanoparticles. *Acc Chem Res* 44(10):947–956.
13. Huang Y, He S, Cao W, Cai K, Liang X-J (2012) Biomedical nanomaterials for imaging-guided cancer therapy. *Nanoscale* 4(20):6135–6149.
14. Blas H, et al. (2008) Elaboration of monodisperse spherical hollow particles with ordered mesoporous silica shells via dual latex/surfactant templating: radial orientation of mesopore channels. *Langmuir* 24(22):13132–13137.
15. Zheng N, Fan J, Stucky GD (2006) One-step one-phase synthesis of monodisperse noble-metallic nanoparticles and their colloidal crystals. *J Am Chem Soc* 128(20):6550–6551.
16. Park S, Lee D (2012) Synthesis and electrochemical and spectroscopic characterization of biicosahedral Au25 clusters. *Langmuir* 28(17):7049–7054.
17. Yang Y, Chen S (2003) Surface manipulation of the electronic energy of subnanometer-sized gold clusters: An electrochemical and spectroscopic investigation. *Nano Lett* 3(1):75–79.
18. Wu Z, Jin R (2010) On the ligand's role in the fluorescence of gold nanoclusters. *Nano Lett* 10(7):2568–2573.
19. Wu X, et al. (2010) Ultrasmall near-infrared gold nanoclusters for tumor fluorescence imaging in vivo. *Nanoscale* 2(10):2244–2249.
20. Frangioni JV (2003) In vivo near-infrared fluorescence imaging. *Curr Opin Chem Biol* 7(5):626–634.
21. Jain PK, Lee KS, El-Sayed IH, El-Sayed MA (2006) Calculated absorption and scattering properties of gold nanoparticles of different size, shape, and composition: applications in biological imaging and biomedicine. *J Phys Chem B* 110(14):7238–7248.
22. Zhu M, et al. (2009) Reversible switching of magnetism in thiolate-protected Au25 superatoms. *J Am Chem Soc* 131(7):2490–2492.
23. Bridot J-L, et al. (2007) Hybrid gadolinium oxide nanoparticles: Multimodal contrast agents for in vivo imaging. *J Am Chem Soc* 129(16):5076–5084.
24. Zhang F, et al. (2012) Mesoporous multifunctional upconversion luminescent and magnetic "nanorattle" materials for targeted chemotherapy. *Nano Lett* 12(1):61–67.
25. Zucker D, Marcus D, Barenholz Y, Goldblum A (2009) Liposome drugs' loading efficiency: A working model based on loading conditions and drug's physicochemical properties. *J Control Release* 139(1):73–80.
26. Liu J, Jiang X, Ashley C, Brinker CJ (2009) Electrostatically mediated liposome fusion and lipid exchange with a nanoparticle-supported bilayer for control of surface charge, drug containment, and delivery. *J Am Chem Soc* 131(22):7567–7569.
27. Chen Y, et al. (2010) Hollow/rattle-type mesoporous nanostructures by a structural difference-based selective etching strategy. *ACS Nano* 4(1):529–539.
28. Gao F, et al. (2012) Doxorubicin loaded silica nanorattles actively seek tumors with improved anti-tumor effects. *Nanoscale* 4(11):3365–3372.
29. Ho YS, McKay G (1999) Pseudo-second order model for sorption processes. *Process Biochem* 34(5):451–465.
30. Fontecave T, Sanchez C, Azaïs T, Boissière C (2012) Chemical modification as a versatile tool for tuning stability of silica based mesoporous carriers in biologically relevant conditions. *Chem Mater* 24(22):4326–4336.
31. Jiang X, et al. (2010) Endo- and exocytosis of zwitterionic quantum dot nanoparticles by live HeLa cells. *ACS Nano* 4(11):6787–6797.
32. Bardhan R, et al. (2009) Nanoshells with targeted simultaneous enhancement of magnetic and optical imaging and photothermal therapeutic response. *Adv Funct Mater* 19(24):3901–3909.
33. Kircher MF, et al. (2012) A brain tumor molecular imaging strategy using a new triple-modality MRI-photoacoustic-Raman nanoparticle. *Nat Med* 18(5):829–834.
34. Bardhan R, Lal S, Joshi A, Halas NJ (2011) Theranostic nanoshells: From probe design to imaging and treatment of cancer. *Acc Chem Res* 44(10):936–946.
35. Beard P (2011) Biomedical photoacoustic imaging. *Interface Focus* 1(4):602–631.
36. Laufer J, et al. (2012) In vivo preclinical photoacoustic imaging of tumor vasculature development and therapy. *J Biomed Opt* 17(5):0560161–0560168.
37. van Gemert MJC, Jacques SL, Sterenborg HJCM, Star WM (1989) Skin optics. *IEEE Trans Biomed Eng* 36(12):1146–1154.
38. Welch AJ, van Gemert MJC (2011) *Optical-Thermal Response of Laser-Irradiated Tissue* (Springer, Berlin).
39. Hirsch LR, et al. (2003) Nanoshell-mediated near-infrared thermal therapy of tumors under magnetic resonance guidance. *Proc Natl Acad Sci USA* 100(23):13549–13554.
40. Kennedy LC, et al. (2011) A new era for cancer treatment: Gold-nanoparticle-mediated thermal therapies. *Small* 7(2):169–183.
41. Liu T, et al. (2011) Single and repeated dose toxicity of mesoporous hollow silica nanoparticles in intravenously exposed mice. *Biomaterials* 32(6):1657–1668.
42. Sonavane G, Tomoda K, Makino K (2008) Biodistribution of colloidal gold nanoparticles after intravenous administration: effect of particle size. *Colloids Surf B Biointerfaces* 66(2):274–280.
43. Hainfeld JF, Slatkin DN, Focella TM, Smilowitz HM (2006) Gold nanoparticles: A new X-ray contrast agent. *Br J Radiol* 79(939):248–253.
44. Benezra M, et al. (2011) Multimodal silica nanoparticles are effective cancer-targeted probes in a model of human melanoma. *J Clin Invest* 121(7):2768–2780.
45. Fehse B, et al. (2000) CD34 splice variant: An attractive marker for selection of gene-modified cells. *Mol Ther* 1(5 Pt 1):448–456.

Downloaded at Palestinian Territory, occupied on December 4, 2021
www.manaraa.com